Local structural mechanism for phase transition and ferroelectric polarization in the mixed oxide math xmlns="http://www.w3.org/1998/Math/MathML">mrow>msub>mi mathvariant="normal">K/mi>mrow>mn>0.5/mn>/mrow>/msub>msub>mi>Na/mi>mrow>mn>0.5/mn>/mrow>/msub>msub>mi>NbO/mi>mn>3/mn>/msub>/mrow>/math>

J. Kong, J. Liu, F. Marlton, M. R. V. Jørgensen, and A. Pramanick

Phys. Rev. B **103**, 184104 — Published 11 May 2021

DOI: 10.1103/PhysRevB.103.184104

Local structural mechanism for phase transition and ferroelectric polarization in mixed-oxide $K_{0.5}Na_{0.5}NbO_3$

J. Kong,[1] J. Liu,[2] F. Marlton,[3] M. R. V. Jørgensen,[4,5] A. Pramanick[1,*]

[1]Department of Materials Science and Engineering, City University of Hong Kong, Hong Kong, China

[2]Neutrons Scattering Division, Oak Ridge National Laboratory, Oak Ridge, TN, USA

[3]Department of Chemistry, University of Sydney, Sydney, NSW, Australia

[4]Center for Materials Crystallography, Department of Chemistry and iNANO, Aarhus University, 8000 Aarhus C, Denmark

[5]MAX IV Laboratory, Lund University, SE-221 00 Lund, Sweden

[*]apramani@cityu.edu.hk

Abstract

$(K_xNa_{1-x})NbO_3$ (KNN) and its solid solutions are considered as potential alternatives to traditional Pb-based piezoelectric materials. Recent investigations indicated that the local structure in KNN is much more complex than its long-range average structure. Here, we have undertaken a systematic investigation of the temperature-dependent evolution of local and average structures of KNN5 ($(K_xNa_{1-x})NbO_3$, x=0.5) using time of flight neutron scattering. Rietveld analysis of neutron diffraction patterns indicated that the average structure of KNN5 changes from monoclinic-to-tetragonal-to-cubic upon heating from 100 to 773 K. In contrast, analysis of neutron pair distribution function (PDF) indicated that the local structure stays monoclinic within the above temperature range. Based on comparative analysis of local and average structures, it is proposed that the average structural phase transitions in KNN5 are partly derived from a local ordering of the polar units, which are correlated over a length of 10~15 Å. A clear indication of order-disorder type transition at 473 K is evident from the temperature-dependent PDF patterns. Additionally, based on local structural analysis, it is shown that large electrical polarization in KNN5 can be attributed to displacements of both A-site and B-site atoms. These structural insights may help in further

optimization of electrical properties of Pb-free KNN piezoceramics.

I. INTRODUCTION

Piezoelectric ceramics, or piezoceramics in short, are widely used in sensors, actuators, ultrasonic transducers, and energy harvesting devices, owing to their exceptional ability for electro-mechanical transduction [1]. Due to their large piezoelectric coefficient and high Curie temperatures (T_c) solid solution of $PbZr_{1-x}Ti_xO_3$ (PZT) [2], and PZT-based ceramics are widely used in many electronic devices [1]. The peak piezoelectric properties in PZT are observed for x = 0.48, which constitutes a morphotropic phase boundary (MPB) [2]. However, since PZT ceramics contain up to 60% Pb by weight, which can cause environmental pollution and accumulate in the human body, various legislations have been passed since 2001 that encouraged research and development (R&D) of lead-free piezoelectric materials [3]. Among the Pb-free candidates, $(K_xNa_{1-x})NbO_3$-based ceramics are considered as a promising class of materials due to their large piezoelectric coefficients and high Curie temperatures T_c in the range of 400~500 °C. For pure $(K_xNa_{1-x})NbO_3$, maximum piezoelectric constant, and high T_c are reported near x=0.5 [4–8], although the underlying reason for such enhancements in properties remains unclear [9]. It was argued that the peak electrical properties for $(K_xNa_{1-x})NbO_3$ near x=0.5 can be attributed to the presence of an MPB [10–12], similar to what is observed for PZT. However, the structural changes across the MPB in $(K_xNa_{1-x})NbO_3$ are very subtle, in contrast to those in PZT. Later, it has been suggested that the enhanced properties in $(K_xNa_{1-x})NbO_3$-based ceramics stem from a polymorphic phase transition (PPT) from orthorhombic to tetragonal (O-T) phase near room temperature [13–15]. Although phase boundaries are considered to play an important role towards the high

piezoelectric properties, the underlying structural complexities have made it difficult to unambiguously determine the microscopic mechanism for phase transitions in $(K_xNa_{1-x})NbO_3$ and their exact role towards the enhanced properties.

The long-range crystallographic structure of in $(K_xNa_{1-x})NbO_3$ solid solutions have been extensively studied in the past. The phase diagram of in $(K_xNa_{1-x})NbO_3$ was reported by Jaffe et al. in 1971 [8], and by Ahtee and Glazer in 1976 [16], which included multiple phases with different oxygen octahedral tilting modes and cation displacements. In general, it was considered that upon heating, $(K_xNa_{1-x})NbO_3$ transforms from rhombohedral (R) to orthorhombic (O) to tetragonal (T), and finally to a cubic (C) phase. Nevertheless, there exists a debate about the crystal structures of different phases in $(K_xNa_{1-x})NbO_3$. For example, recent works revealed that the crystal structure of $K_{0.5}Na_{0.5}NbO_3$ at room temperature can be described as monoclinic with *Pm* space group, instead of the traditionally considered orthorhombic *Amm2* space group [17-22]. Gupta et al. pointed out that the transformation from *Amm2* to *Pm* suggests a loss of mirror plane and a two-fold axis, which primarily arise due to a mismatch in the ionic radii of K^+ (1.64 Å) and Na^+ (1.39 Å) [23,24]. Since the A-site is partially occupied by Na^+ and K^+, the A-O bond distance is not homogeneous in $(K_xNa_{1-x})NbO_3$ [25,26]. Consequently, the structure in $(K_xNa_{1-x})NbO_3$ is more disordered as compared to the end members $KNbO_3$ and $NaNbO_3$, with pronounced crystallographic distortions at short length scales ~ 10 Å [21,23].

Therefore, to understand the “structure-property” relationship for such mixed oxide compositions, characterization of the average structure from analysis of Bragg diffraction alone may not be sufficient. Instead, the pair distribution function (PDF), which informs about

the pairwise atomic correlations as a function of interatomic distance, *r*, is a useful method for characterizing the local atomic structure [27]. Experimentally, PDF is obtained from Fourier transformation of X-ray/neutron total scattering patterns (contain information of both Bragg and diffuse scattering). Since no requirement for translational symmetry is imposed *a priori* in this method, PDF is particularly sensitive to the local scale atomic correlations, which are not discernable from analysis of the Bragg diffraction peaks alone. In the past, the application of the PDF method revealed unique local structural information in many ferroelectric materials. For example, Egami et al. showed for Pb-based ferroelectrics, such as Pb(Zr, Ti)O_3, Pb(Sc, Ta)O_3, and Pb(Mg, Nb)O_3 [28–30], the local bonding environment of Pb^{2+} remains unchanged up to 1000 K, even though there are multiple phase transitions characterizing changes in the average crystal structure [31]. Similar differences between local and average structures were also observed for Pb-free ferroelectrics, such as $NaNbO_3$, $Na_{0.5}Bi_{0.5}TiO_3$, and $BaTiO_3$[32-34]. Recent PDF studies on KNN also indicated significant differences between the local and average atomic structures, which are caused due to difference in the ionic sizes of K^+ and Na^+ that leads to oxygen octahedral tilting disordering [21,26]. Especially, the local structure of KNN within 20 Å is different from the average crystal structure [21]. Nevertheless, a comparative analysis of the evolution of the average and local structures as a function of temperature in KNN is lacking, which is necessary to better elucidate the origin of enhanced properties at certain phase boundaries.

Here, we have systematically studied the structural evolution in KNN5 ($(K_xNa_{1-x})NbO_3$, x=0.5) at different length scales from 100 to 773 K. The average long-range structure, as a function of temperature, was analyzed by Rietveld refinement of neutron powder diffraction patterns, while the local structure was analyzed from neutron total scattering patterns and

PDF analysis. Our analysis indicates that although the long-range average structure undergoes three different phase transitions upon heating from 100 to 773 K (monoclinic to tetragonal to cubic), the local structure up to ~10 Å length scale remains monoclinic at all temperatures. Furthermore, the local monoclinic structure retains a polar character due to octahedral distortions, and this local polarization acts as a driving force for long-range structural ordering. A structural evolution model is proposed in which the average long-range phase transitions in KNN5 are a consequence of increasing local scale atomic (dis)order. Additionally, it is shown that large ferroelectric polarization in KNN5 results from displacements of both A-site and B-site ions. These results provide insights into the local atomistic mechanisms for multiple phase transitions in KNN5 and elucidate the origin of large functional properties near the different phase boundaries.

II. EXPERIMENT

A. Materials preparation

$K_{0.5}Na_{0.5}NbO_3$ (KNN5) powders were prepared by a traditional solid-state reaction. K_2CO_3 (Sigma Aldrich, 99.7 %), Na_2CO_3 (Sigma Aldrich, ~100 %), and Nb_2O_5 (Sigma Aldrich, 99.9 %) were ball-milled in ethanol for 24 hours. The mixed powder slurry was dried and then calcined at 800 ℃ for 4 hours. Then the calcined powder was ball-milled for another 24 hours, dried and calcined again at the same condition. After a second ball-milling, the dried powders were ground, mixed with polyvinyl alcohol (PVA), and sieved through 100 μm mesh. Then the granulated powders were pressed into pellets of diameter 10 mm and thickness 1 mm with a pressure ~ 34.5 MPa. The pellets were placed in an alumina crucible and sintered in air at 1100 ℃ for 4 hours. During sintering, the green pellets were covered with powders

of the same composition KNN5, to compensate for the volatilization of certain elements. The sintered pellets were then grounded, and the obtained powder was sieved through 100 μm mesh to get fine uniformly sized powder for neutron diffraction and differential scanning calorimetry (DSC) experiments.

B. Materials characterization

Time of flight neutron scattering experiments were performed at the NOMAD BL1B instrument of the Spallation Neutron Source (SNS). The powdered sample was loaded into a vanadium can of diameter ~6 mm for the data collection on the automatic shifter. A cobra cryostream was used to control the temperature from 100-290 K. Data at higher temperatures (373 – 773 K) were collected in an ILL furnace. Powder samples were filled into the standard NIST vanadium can with a diameter of 6 mm. Two ~24 min datasets were collected at each temperature, which were then summed together to improve the measurement statistics. For each temperature, background intensity measured from an empty vanadium can was subtracted from the neutron scattering intensity from the sample. The background corrected intensity was subsequently normalized against signal from a 6 mm vanadium rod to correct for detector efficiency. The thermal analysis of the powder samples was done on a differential scanning calorimetry instrument (DSC 404 F3, Netzsch) at a heating rate of 10K/min.

III. RESULTS AND DISCUSSION

A. Average structure analysis of KNN5

Fig. 1(a) shows the neutron diffraction patterns of KNN5 ceramic powders as a function of temperature from 100 K to 773 K. All the diffraction peaks could be indexed using KNN5

perovskite phases, with the presence of a small amount of (<1%) undetermined secondary phase. The neutron diffraction patterns at 773 K and 673 K were indexed based on an ideal cubic structure with the space group $Pm\bar{3}m$. At 573 K, the (220), (311), (320), (400), (420), and (422) peaks are split (marked with arrows), which indicates a non-cubic phase at this temperature. Another change in the above *hkl* peak profiles is apparent at ~373 K, such as for the (220) peak, the shoulder at higher Q disappears and another shoulder appears at a lower Q value. This indicates a structural transition to a lower symmetry phase below 473 K. Fig. 1(b) shows heat flow measured using differential scanning calorimetry (DSC) during heating the powder samples over 400 K~800 K. The peaks in the DSC curve indicate phase transitions at T ~ 471 K and T ~ 674 K, which is consistent with the changes in different *hkl* diffraction peak profiles shown in Fig. 1(a) at these temperatures. The phase transition at T ~ 674 K is consistent with the earlier reported phase diagram of KNN [8,19,20], which indicated a tetragonal-to-cubic phase transition upon heating at this temperature, as shown in Figure 1(c). Based on earlier studies, the DSC peak at T ~ 471 K can be attributed to a transition from tetragonal to either monoclinic [20,22] or orthorhombic [8] phase.

To resolve the average long-range structural phases in KNN5, the temperature-dependent neutron diffraction patterns were analyzed by Rietveld refinement using the software General Structure Analysis System (GSAS II) [35]. The structural parameters, viz. unit cell constants, atomic coordinates, and atomic displacement parameters were refined against the experimental data. During refinement, the structural coordinates and atomic displacement parameters were constrained to be identical for K and Na atoms, since refining them separately resulted in unstable refinement. The quality of the fits was assessed based on weighted residuals R_w [36]. To check the stoichiometry, after refining all the structural

parameters, the occupancies for A-site cations, K^+ and Na^+, were refined (given the constraint that the total occupancy should be 1), which provided values of 0.486(5) and 0.513(5), respectively. Since the deviation from the nominal composition was very small, the occupancies were subsequently fixed at 0.5 for refinement of other structural parameters.

A cubic *Pm$\bar{3}$m* structure model was used to refine the experimental data at 773 K and 673 K, for which the obtained R_w was 4.87 % and 5.80 %, respectively. The experimental and calculated diffraction profiles are shown in Figs. 2(a) and 2(b). At 573 K, a tetragonal *P4mm* structure model provides the best fit to the diffraction pattern, yielding an R_w of 4.98% was obtained (Fig. 2(c)). At the phase transition temperature of T ~ 473 K, the diffraction pattern could not be satisfactorily fitted using a single-phase model, which is further addressed below. All the diffraction patterns measured at or below 373 K (shown in pink and red in Fig. 1) appear to be similar, which indicates no change in the average crystal structure occurs below this temperature. However, earlier studies variously described the room-temperature structure of KNN5 as either monoclinic (*Pm* space group) [20] or orthorhombic (*Amm2* space group) [8]. To resolve this issue, we compared the Rietveld refinement fits using either *Pm* or *Amm2* space group. The experimental and calculated profiles using the *Pm* space group are shown in Fig. 2(f); the corresponding fit using the *Amm2* space group is shown in Fig. S1(a). The relatively lower R_w obtained for the *Pm* model (R_w of 4.48 %) over that of the *Amm2* model (R_w of 4.94 %) indicates the appropriateness of the former. More importantly, it was observed that the individual *hkl* peaks were better reproduced using the *Pm* space group, such as the (320) reflection shown in the inset of Figure 2(f). This was also observed for the diffraction patterns measured at 373 and 100 K (Figs. 2(e) and 2(g)) (*Amm2* see Fig. S1(b,c) in the Supplementary Information) [37].

For the diffraction pattern measured at 473 K, the best fit was obtained using a two-phase "*Pm +P4mm*" model, as shown in Fig. 2(d). Instead, using only a single tetragonal phase *P4mm* space group led to a significantly worse fit with a correspondingly high R_w of ~7.52% (see Supplementary Information for details) [37]. It can therefore be concluded that both monoclinic and tetragonal phases coexist at 473 K, which may explain the enhanced piezoelectric properties at the phase transition temperature of T_{T-M} ~ 473 K [3].

Note that the neutron diffraction patterns were recorded using all six banks of NOMAD. The diffraction data of the middle four banks (2θ = 31°, 67°, 122°, and 154°) were fitted simultaneously. Fig. 2 only shows the neutron diffraction patterns from BANK 5 of the instrument, which has the highest resolution. The diffraction data and corresponding fits from the other BANKs are shown in the Supplementary Information (Figs. S2, S3, and S4) [37]. The refined structural parameters such as unit cell constants, atomic coordinates, and thermal factors at various temperatures are shown in Table 1. The average structural parameters as a function of temperature are plotted in Fig. 3(a-d). While the lattice constants *a* and *c*, exhibit discontinuous changes at the tetragonal-to-monoclinic phase transition temperature T_{T-M}, *b* increases gradually with an increase in temperature from 100 to 773 K. Similarly, as shown in Fig. 3(d), β for the long-range average structure remains slightly higher than 90° below 473 K, but approaches 90° above 473 K. In the next section, we will compare the temperature-dependent changes in the long-range average structural parameters with that of local structural changes determined from analysis of neutron PDF.

B. Local structure analysis of KNN5

Since earlier works indicated a difference in local and average structures of KNN, we

investigated the local structure using the neutron pair distribution function (PDF). The pair distribution function G(*r*) is calculated from the sine Fourier transformation of the time-of-flight neutron total scattering data. PDFs for KNN5 at 100 K~773 K in the range of *r* ~ 1.7-40 Å are shown in Fig. 4(a). We did PDF fits of G(*r*) at different temperatures for r~1.7~40 Å using structural parameter from Rietveld refinement as a starting point, shown in Fig.S5. It was indicated that the local and average structure of KNN5 approach each other at a longer distance ~40 Å (see Supplementary Information for details) [37]. Moreover, in Fig. 4(a), it is evident that the PDF peak profile changes most significantly within *r* ~1.7-3 Å with temperature over the range of 100 K~773 K. Therefore, to further explore the length scale-dependent structural evolution, a "box-car" type refinement was carried out. This method was earlier used to characterize the lattice parameters variation at different length scales in Pb-free ferroelectrics such as refs. [38,39]. All refinements were carried out using the software PDFgui [40].

The box-car fitting of KNN5 was done at 100 K since the amplitude of atomic thermal vibrations are small and thus the atomic positions could be determined more accurately at this temperature. The starting parameters for the box-car fitting was obtained from the Rietveld refinement results of the long-range average structure at 100 K using the *Pm* space group, as discussed above. A size of 10 Å for fitting boxes and a step size of 2.5 Å were used for box-car fitting of the G(*r*) patterns in the range from 1.7 to 40 Å. The lattice parameters *a*, *b*, *c*, and angle β of the monoclinic unit cell was adjusted, together with the thermal parameters, until the best possible fit to the experimental data was achieved. The quality of the fits was assessed visually and from the values of the weighted residuals R_w. Figs. 4(b-c) shows measured and calculated neutron G(*r*) profiles at 100 K in the range of *r*

~ 1.7-10 Å and *r* ~ 30-40 Å. The G(*r*) profiles for other *r* ranges are shown in Figs. S6, which shows that all the experimental G(*r*) could be fit well using the *Pm* space group. The residual factors R_w are in an acceptable range of 6%~13%. Fig. 4(d-e) shows evolution of the structural parameters as a function of *r* at 100K in the range of *r* ~ 5 to 35 Å, which are obtained from box-car refinement. As shown in Fig .4(d), the lattice parameters a,b ,and c obtained from fitting of G(*r*) at low *r* (first box, 1.7~10 Å) are significantly different from those obtained from Rietveld refinement of the Bragg diffraction peaks, which demonstrates the difference between the local and average structures. However, the lattice parameters obtained from the analysis of G(*r*) and Rietveld refinement of Bragg diffraction patterns approach each other beyond *r* ~ 10~15 Å, which indicates that the local structural distortions average out beyond this length scale. Additionally, as shown in Fig. 4(e), while the values of β obtained from fitting of the G(*r*) within *r* ~10 Å are significantly higher than the average β value, they converge beyond *r* > 15 Å. The current results are consistent with the study of Petkov et al., which indicated a convergence between local and average structures occurs beyond 2 nm length scales for KNN [21].

To characterize the local structural evolution with temperature, the temperature-dependent *G*(*r*) in the range of *r* ~ 1.7-10 Å were next investigated. Fig. 5 shows *G*(*r*) in the range of r ≤ 4 Å, as a function of temperature from 100 K to 773 K. The r ≤ 4 Å region indicates the short-range correlations for nearest neighbor and next-nearest neighbor interatomic distances. In Fig. 5, the first arrow represents Nb-O interatomic distance, and the next two arrows represent the K/Na-O interatomic distance for a typical perovskite structure. For the Nb-O bond, there exists a clear splitting below 473 K, which indicates that the local octahedra are more distorted below 473 K. To explore the local distortion evolution,

we fitted the measured G(*r*) at different temperatures. Both *Pm* and *Amm2* structural models were examined for the fitting of the G(*r*) measured at 100 K, as shown in Figs. 6 (a) and Fig. S7. The *Pm* model (R_w ~7.24%) provided a better fit to the data as compared to the *Amm2* model (R_w ~8.57%). Particularly, the peaks at r ~2.8 Å and 4.9 Å were better reproduced using the *Pm* model. Similar results were obtained for G(*r*) at 290 K and 373 K, as shown in Figs.6(b-c) and Fig.S8-S9. For temperatures at or above 473 K, for which the average long-range structure is transformed to tetragonal, the Nb-O peak appears broad and asymmetric in Fig. 5, indicating a breaking of the 6-fold degeneracy of the Nb-O bond distance [25]. It is therefore apparent that the local structure of KNN5 for temperatures 473~773 K (blue line group) cannot be accurately described by a cubic model, even at the highest temperature ~773 K. At the phase transition temperature T_{T-M} ~473 K, the *Pm* space group could better reproduce the experimental G(*r*) as compared to *Amm2* and *P4mm* structure models, especially with respect to the peaks at r ~2 Å and 2.8 Å, as shown in Fig. 6(d) and Fig. S10(a-c). For the measured G(*r*) above 473 K, *Pm* yielded a superior fit compared to other models: *P4mm* or (and) $Pm\bar{3}m$ (Figs.6(e-g) and Figs.S11-S13). This was especially obvious for the peak at ~4Å which was described satisfactorily by the *Pm* model as well as yielded lower R_w values compared to the other higher symmetry models.

Based on the above analysis, it is therefore apparent that the local structure for $r < 10$ Å in KNN5 exhibits monoclinic distortion with *Pm* space group at all temperatures from 100 K to 773 K, although the long-range average structure exhibits three different phase transitions from 100 K to 773 K. The coexistence of a lower symmetry local and a higher symmetry average atomic arrangement is not an unusual picture and has been observed earlier in $BaTiO_3$ [34].

The refined structural parameters (unit cell constants, atomic coordinates, and thermal factors) for the local structure within r ~ 1.7-10 Å using *Pm* space group for temperatures 100~773 K are shown in Table 1. A comparison of the temperature-dependent local and average structural parameters is provided in Figs. 3. Interestingly, in contrast to the average structure, *b* for the local structure reaches a maximum value, and the slope of the β significantly changes near the monoclinic-tetragonal phase transition, T_{T-M} ~ 473 K. This result is similar to the proposed composition-dependent evolution of structural parameters in $K_xNa_{1-x}NbO_3$, whereby an abrupt change in slope of the β occurs at x~0.20, which delineates regions with slightly different crystal structures [7]. Notably, in correlation to the inflection points for the local structural parameters (Figure 3(b,d)), we note a distinct change in the G(*r*) profiles at T_{T-M}, as shown in Figure 5. Specifically, for temperatures below 473 K, the peaks representing the Nb-O nearest-neighbor correlations become sharper, indicating that the structure becomes more ordered below this temperature. Therefore, the reversal in trends for temperature-dependent evolution in b and β (shown in Fig. 3) are likely correlated to an order-disorder type transition at this temperature, which is further discussed below.

C. DISCUSSION

C.1. Nature of structural phase transitions in KNN5

Phase transitions in perovskite ferroelectrics, such as $BaTiO_3$ and $KNbO_3$, have been shown to exhibit both displacive and order-disorder type characteristics [41-44]. As per the displacive model, the direction of the B-site atomic displacements changes at a phase transition point, such as from <110> type displacements in the orthorhombic phase to <001> type displacements in the tetragonal phase. In contrast, according to the order-disorder

model, the B-site cation is always locally displaced along the <111> directions, while the average structure changes are due to partial re-ordering of the local B-site displacements. To elucidate the characteristic of the phase transitions in KNN5, we analyze below the details for Nb displacements as a function of temperature.

Based on Rietveld refinement of the Bragg peaks as well as analysis of G(*r*), the fractional displacements of Nb at different temperatures from its high symmetry position are shown in Fig 7(a-b) (see Supplementary Information Fig.S14 for details of calculation process) [37]. The components of Nb displacements along both the $[\bar{1}00]$ ($S_{\bar{1}00}$) and $[001]$ (S_{001}) directions are indicated in Fig.7(a). The fractional displacements S_{001} are slightly higher than $S_{\bar{1}00}$, which is consistent with the Nb displacement direction reported by Petkov et al [21]. The variation in net fractional displacements approximately parallel to the $[\bar{1}01]$ or [001] direction as a function of temperature is shown in Fig. 7(b). The inset in Fig. 7(b) illustrates the net displacements of Nb at 100 K and 773 K, in which Nb displacements are exaggerated for clarity. In the average structure, the Nb off-center displacements decrease in magnitude with increasing temperature on the whole, except for an abrupt change at $T_{T\text{-}M}$~473 K because of two-phase coexistence. In contrast, Nb displacements in the local structure decrease continuously with temperature.

Octahedral distortion due to Nb off-centering can be calculated from the Nb-O bond lengths determined from structural analysis, using the following equation:

$$D = \frac{1}{n}\left[\sum_i^n \left(\frac{d_i - d}{d}\right)^2\right] \quad (1)$$

where n is the coordination number (in this case n=6), and d_i and d are the individuals and average values of the interatomic distances in polyhedral, respectively [45]. The calculated

octahedral distortion parameters versus temperature are shown in Figure 7 (c). The navy line indicates the values for D calculated using Nb-O bond lengths determined from Rietveld analysis of the Bragg diffraction patterns, while the pink line indicates the same determined from analysis of G(*r*). A discontinuity in the average octahedral distortion is evident at $T_{T\text{-}M}$ ~ 473 K, while the local octahedral distortion changes gradually as a function of temperature. Graphical representations of the Nb-O bond length within the oxygen octahedra are provided in Figs.7(d-g). The apical O atoms and the O atoms within the basal plane of the octahedra are marked as red O_{ap} and pink O_{bas}, respectively. In Figs.7(d) and 7(f), at 100 K, there is an insignificant Nb displacement towards one of the O_{ap} with an equal Nb-O_{ap} bond length of ~1.98(9) Å. Instead, Nb is displaced towards one of the basal edges of the octahedron, which aligns with the direction of spontaneous polarization, leaving two groups of Nb-O_{bas} bond lengths: ~1.85 Å and~ 2.14 Å for the local structure (Fig.7(d)), and 1.87 Å and 2.12 Å for the average structure (Fig.7(f)). Therefore, at 100 K, the apparent Nb off-centering is ~0.14 Å for the local structure and~0.12 Å for the average structure. The octahedral distortion parameters in the local and average structures are in Fig. 7(c). At 773 K, for the local structure, there is a slight difference among the Nb displacements towards the O_{bas} and O_{ap} as depicted in Fig.7(e), which results in a small but non-zero value of D at 773 K in Fig.7(c). In contrast, for the average cubic structure at 773 K, all the Nb-O bonds length are ~1.99 Å as depicted in Fig.7(g), and there is no off-centering of Nb within the oxygen octahedra, which leads to D = 0 in Fig.7(c).

The spontaneous polarization (P_s), resulting from octahedral distortion is estimated from the following relation:

$$P_S = \frac{e}{V_C}\sum_i z_i{}'' \Delta_i \quad (2)$$

where V_c is the unit cell volume, Δ_i is the shifts of the *i*th atom along the ferroelectric axis, z_i'' is the apparent charge [46,47]. Fig.8 (a-b) shows the calculated spontaneous polarization (P_s) as a function of temperature for the average and local structure, respectively. The values calculated here for the polarization are consistent with those reported earlier [48]. In Fig.8 (a), the average P_s decreases discontinuously while local P_s decreases continuously with increasing temperature. This can be rationalized based on a change in the ordering of the local dipoles at the phase transition temperature of $T_{T\text{-}M}$ ~ 473 K. An order-disorder transition is also supported from the temperature-dependent G(*r*) profiles shown in Figure 5. In Fig. 5, the Nb-O peak at T≤373 K is split with peak centers at ~1.89 Å and ~2.13 Å, while for T≥473 K, the Nb-O peak appears asymmetric but without a clear split within the experimental resolution, which indicates that the Nb displacements become more disordered above $T_{T\text{-}M}$ ~ 473 K. This is consistent with previous studies, which concluded an order-disorder characteristics of phase transition in ferroelectric perovskites [41,42].

In fact, an order-disorder type of transformation has been reported for the end members of $KNbO_3$ and $NaNbO_3$[32,43-44]. For $KNbO_3$, the sequence of phase transitions from rhombohedral-to-orthorhombic-to-tetragonal-to-cubic occurs due to incremental disordering of the Nb displacements [43,44]. In comparison, for $NaNbO_3$, Nb always displaced along <111> directions, while the different average phase transitions are due to the ordering of the oxygen octahedral tilts [32]. Based on a comparison of the temperature-dependent local and average structures of KNN5, the polarization within the local monoclinic units in KNN5 are all directed along the same $\left[\bar{1}01\right]$ direction, which can be compared to the average

orthorhombic phase of $KNbO_3$. Therefore, the average phase transition sequence of monoclinic-tetragonal-cubic in KNN5 can be described as a disordering of the local monoclinic units by cooperative displacement of K/Na and Nb atoms relative to the oxygen network, similar to scenarios described in [43,49]. A scheme of order-disorder transition in KNN5 is shown in Fig.8 (c-e). As illustrated in Fig.8 (c), in the monoclinic phase, the local Nb displacements (solid circle) are oriented approximately along $[\bar{1}01]$ direction in the *a-c* plane with $\phi \approx 45°$, where ϕ is the angle between atom displacement direction and the [001] direction. Since the local polarization directions along $[\bar{1}01]$ are highly ordered at low temperatures, the resultant atomic displacement (open circle) in the average structure is also along $[\bar{1}01]$. At higher temperatures, the Nb displacements become more disordered. As illustrated in Fig.8 (d), above 473 K, the Nb displacements are disordered along $[\bar{1}01]$ (position 1) and [101] directions (position 2) in the *a-c* plane, which results in an average Nb displacement along the [001] and therefore leads to an average tetragonal structure. With increasing temperature, the Nb atoms are displaced along four directions: $[\bar{1}01]$ (position 1), [101] (position 2), $[\bar{1}0\bar{1}]$ (position 3), and $[10\bar{1}]$ (position 4) in the *a-c* plane, such as illustrated in Fig. 8(e), which results in a cubic average structure with no net polarization.

The driving force for long-range structural ordering in KNN5 is imparted by the polarizing force of the short-range polar units within ~15 Å, similar to the situation that was reported for $BaTiO_3$ and $Ba_xSr_{1-x}O_3$[34]. With increasing temperature, the driving force provided by the local polar units becomes weaker because of decreasing octahedral distortion. At the same time, the required driving force for long-range structural ordering becomes higher due to increased thermal vibrations. At temperatures below 473 K, the driving force is strong enough for the ordering of the long-range structure to an average monoclinic *Pm* phase due

to the large octahedral distortion, as shown in Fig. 7. However, for temperatures above 473 K, the driving force is not enough to transform the long-range structure into a monoclinic phase as compared to the polarizing force of the local polar units due to lower octahedral distortion, as shown in Figure 7. In this situation, the KNN5 average structure transforms into a tetragonal *P4mm* space group above 473 K. For temperatures above~ 673 K, the driving force provided by polar units is too weak due to a very low octahedral distortion and consequently, the long-range structure becomes cubic.

C.2. Origin of ferroelectric polarization in KNN5

The origin of the overall ferroelectric polarization in KNN5 can be characterized by the relative displacements of K/Na and Nb with respect to the oxygen polyhedral distortions. The polarization originating from Nb displacements are presented in section C. 1. Here, we take a closer look at the K/Na displacements. As shown in Fig. 5, there appears an additional peak at ~2.5 Å and a shoulder at ~3.2 Å of K/Na-O bond at low temperature, which can be explained as a result of the displacement of K/Na ions within the AO_{12} dodecahedron. The current observation is similar to that reported earlier by Jiang et al. [32], which also showed a three-way splitting of the Na-O at r = 2.4, 2.8, and 3.1 Å due to Na off-centering displacement in $NaNbO_3$. For KNN5, the off-centering displacement of K/Na is difficult to characterize at high temperatures due to the higher thermal parameters. However, at 100 K, the amplitude of the thermal vibration of K/Na becomes relatively smaller, which leaves a window to determine K/Na off-centering more precisely based on the neutron total scattering data.

From the analysis of the G(*r*) profiles, the off-centered displacement of K/Na in KNN5

at 100 K is ~0.15 Å, which is ~0.25 Å smaller than the ~0.4 Å displacement of Na in $NaNbO_3$ [32]. It can be noted that the ionic radius of K^+ is larger than that of Na^+ by ~ 0.25 Å [24], which reduces the average off-centering of the A-site ions in KNN5 as compared to that in $NaNbO_3$. According to Jiang et al., the energy barrier for atomic motion between the off-centered positions is higher for Na^+ in $NaNbO_3$ due to the rather high displacement of ~ 0.4 Å [32]. Since the average K/Na displacement of ~ 0.15 Å is comparatively lower in KNN5, the energy barrier for atomic motion is also correspondingly reduced. This facilitates easier mobility of the A-site ions in KNN5 on average and therefore leads to greater ferroelectric switching. In other words, the origin of enhanced ferroelectricity in KNN5 as compared to $NaNbO_3$ can be attributed to the improved mobility of the A-site alkali ions, which in turn is caused by partial replacement of Na^+ with K^+. Therefore, the enhanced ferroelectric polarization in KNN5 originates from reorientable off-centered displacements of both A and B site atoms.

IV. CONCLUSION

In summary, we have elucidated the local atomistic mechanism for phase transitions and ferroelectric polarization in KNN5 based on a detailed analysis of temperature-dependent neutron Bragg diffraction and pair distribution function patterns. Analysis of the neutron diffraction patterns indicated that the structure of KNN5 transformed from monoclinic-to-tetragonal-to-cubic with increasing temperature from 100 to 773 K. In contrast, analysis of the neutron pair distribution function indicates that the local structure within ~ 10 Å stays monoclinic over the same temperature range. We show evidence for an order-disorder type of transition at T_{T-M}~ 473 K, which stems from a competition between the

polarizing force of the local monoclinic polar units and increased thermal vibrations at higher temperatures. Besides, based on an analysis of the local atomic structure, we show that large ferroelectric polarization in KNN5 can be attributed to displacements of both A-site K/Na and B-site Nb ions relative to the oxygen polyhedra.

Acknowledgments
Funding support from CityU (Projects No. 7005121 and 6000688) and Research Grants Council of HK (Project No. 9043039) are gratefully acknowledged. FM and MRVJ thank the Danish Agency for Science, Technology, and Innovation for funding the instrument center DanScatt. Affiliation with the Center for Integrated Materials Research (iMAT) at Aarhus University is gratefully acknowledged. JK and FM gratefully acknowledge Michelle Everett for assisting with measurements at the NOMAD instrument. Research conducted at the NOMAD beamlines at ORNL's Spallation Neutron Source was sponsored by the Scientific User Facilities Division, Office of Basic Sciences, U.S. Department of Energy.

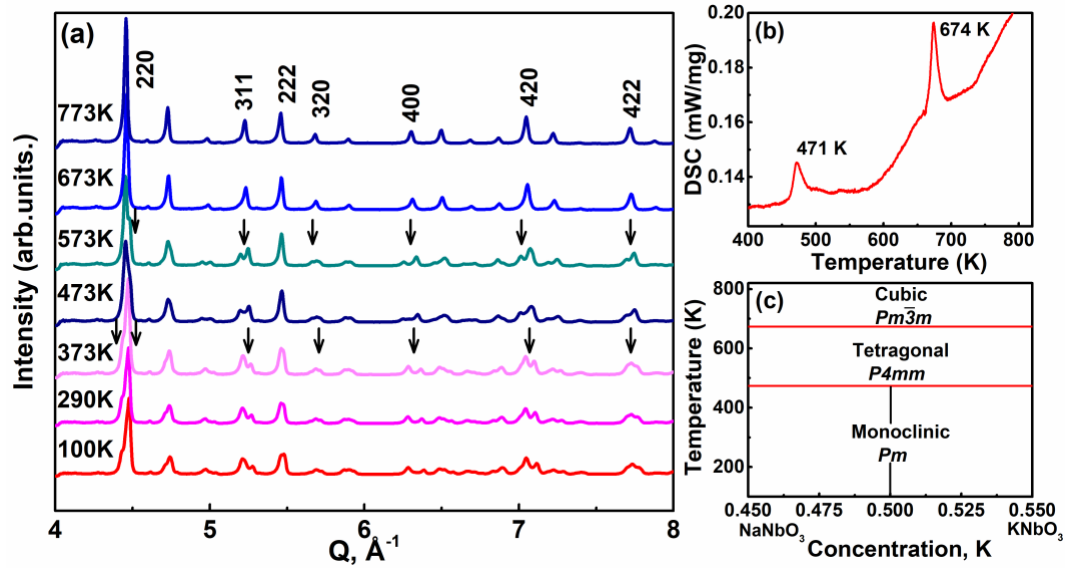

Figure 1

(a) Evolution of the neutron diffraction patterns of $K_{0.5}Na_{0.5}NbO_3$ (KNN5) as a function temperature from 100 to 773 K. The x-axis refers to the wave transfer vector **Q**. h k l reflections are indexed based on a cubic perovskite structure. The arrows mark changes in h k l peak profiles, which indicate phase transitions. (b) Differential scanning calorimetry (DSC) profile for KNN5 powder from 400 K to 800 K, showing endothermic peaks marking the onset of phase transitions behavior on heating. (c) Phase diagram for $K_xNa_{1-x}NbO_3$, showing phase evolution with temperature. KNN5 undergoes a monoclinic-to-tetragonal phase transition at T ~ 471K-473 K and a tetragonal-to-cubic phase transition at T ~ 673 K-674K.

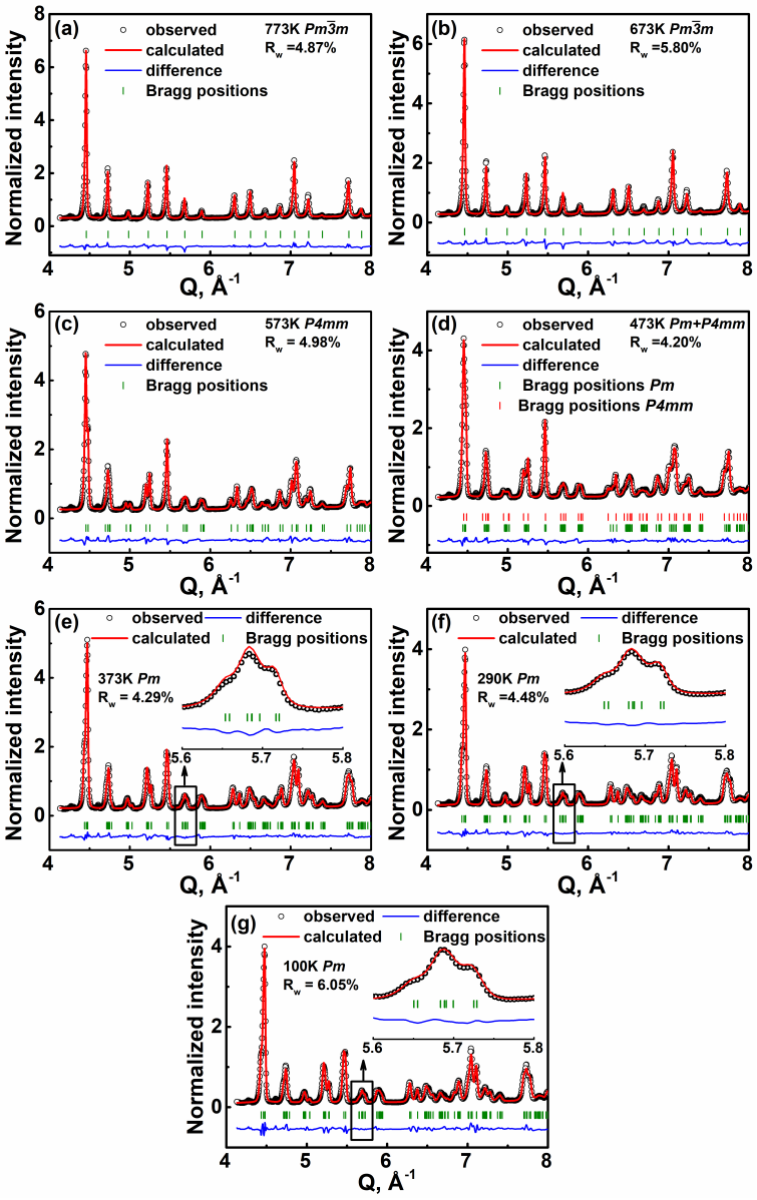

Figure 2

Diffraction patterns of KNN5 powder at different temperatures showing measured (black symbol), refined (red line), difference (blue line) profiles, and Bragg positions (green ticks). The data shown is from BANK 5 of the NOMAD instrument. The Rietveld refinements were carried out using the software GSAS II. (a) Refinement using *Pm$\bar{3}$m* at 773K; (b) Refinement using *Pm$\bar{3}$m* at 673K; (c) Refinement using *P4mm* at 573K; (d) Refinement using two phases *P4mm* and *Pm* at 473K; (e) Refinement using *Pm* at 373K; (f) Refinement using *Pm* at 290K; (g) Refinement using *Pm* at 100K. Weighted residuals R_w are shown for all the refinements. The insets in (e-g) show a comparison between experimental (symbols) and calculated (line) peak profiles for the 320 reflection.

TABLE 1. Structural parameters, fractional atomic coordinates and equivalent isotropic displacement parameters (U_{iso} in Å^2) from the Rietveld refinement and 1.7-10 Å range PDF fit results of neutron data of KNN5 at various temperatures.

Rietveld and PDF refinement of KNN5 at 773 K

Rietveld refinement cubic phase ($Pm\bar{3}m$)					PDF refinement monoclinic phase (Pm)			
Atoms	X	Y	Z	U_{iso}	X	Y	Z	U_{iso}
K/Na	0	0	0	0.0338(3)	-0.0105(160)	0	0.0429(76)	0.0301(52)
Nb	0.5	0.5	0.5	0.0103(2)	0.5050(110)	0.5	0.5120(55)	0.0137(16)
O1	0.5	0.5	0	0.0338(3)	0.5183(68)	0.5	-0.0034(83)	0.0117(30)
O2					0.0086(130)	0.5	0.4783(90)	0.0244(47)
O3					0.4802(70)	0	0.4983(99)	0.0144(35)
Lattice parameter (Å)					Lattice parameter (Å)			
a=b=c=3.9848(1)					a=4.0215(69)			
α=β=γ=90°					b=3.9511(59)		α=γ=90°	
					c=4.0220(72)		β=91.983(290)	

Rietveld and PDF refinement of KNN5 at 673 K

Rietveld refinement cubic phase ($Pm\bar{3}m$)					PDF refinement monoclinic phase (Pm)			
Atoms	X	Y	Z	U_{iso}	X	Y	Z	U_{iso}
K/Na	0	0	0	0.0296(4)	-0.0252(140)	0	0.0476(75)	0.0275(44)
Nb	0.5	0.5	0.5	0.0097(2)	0.4917(62)	0.5	0.5277(31)	0.0115(14)
O1	0.5	0.5	0	0.0170(2)	0.4998(68)	0.5	-0.0015(40)	0.0060(15)
O2					0.0052(71)	0.5	0.4907(100)	0.0217(39)
O3					0.4663(66)	0	0.5021(90)	0.0160(33)
Lattice parameter (Å)					Lattice parameter (Å)			
a=b=c=3.9795(1)					a=4.01873 (63)			
α=β=γ=90°					b=3.9487(55)		α=γ=90°	
					c=4.0199(69)		β=91.8464(260)	

Rietveld and PDF refinement of KNN5 at 573 K

Rietveld refinement tetragonal phase (*P4mm*)					PDF refinement monoclinic phase (*Pm*)			
Atoms	X	Y	Z	U_{iso}	X	Y	Z	U_{iso}
K/Na	0	0	0.0152(10)	0.0281(3)	-0.0038(150)	0	0.0385(64)	0.0225(34)
Nb	0.5	0.5	0.5156(2)	0.0065(2)	0.4756(39)	0.5	0.5284(26)	0.0122(12)
O1	0.5	0.5	0.0490(5)	0.0157(4)	0.4993(55)	0.5	-0.0012(32)	0.0055(10)
O2	0.5	0	0.5571(2)	0.0115(2)	0.0005(40)	0.5	0.4922(68)	0.0148(19)
O3					0.4522(40)	0	0.5012(76)	0.0186(27)
Lattice parameter (Å)					Lattice parameter (Å)			
a=b=3.9644(1)					a=3.9894(61)			
c=4.0134(1)					b=3.9721(51)		α=γ=90°	
α=β=γ=90°					c=4.0051(62)		β=91.2571(310)	

Rietveld and PDF refinement of KNN5 at 473 K								
Rietveld refinement two-phases coexistence phase 1(*Pm*)					PDF refinement monoclinic phase (*Pm*)			
Atoms	X	Y	Z	U_{iso}	X	Y	Z	U_{iso}
K/Na	-0.0003(29)	0	0.032(4)	0.0082(12)	-0.0001(100)	0	0.0597(42)	0.0151(35)
Nb	0.4754(13)	0.5	0.5515(13)	0.0049(9)	0.4769(23)	0.5	0.5317(20)	0.0095(12)
O1	0.5328(10)	0.5	0.0391(21)	0.0157(16)	0.5091(55)	0.5	-0.0012(26)	0.0059(12)
O2	-0.011(3)	0.5	0.5422(20)	0.0142(14)	0.0062(28)	0.5	0.5065(110)	0.0206(28)
O3	0.4869(14)	0	0.5080(8)	0.0054(11)	0.4897(58)	0	0.4933(56)	0.0100(18)
Lattice parameter (Å)					Lattice parameter (Å)			
a=4.0019(3) b=3.9545(2) c=3.9812(2)					a=3.9559(52)			
α=γ=90° β=90.272(4)					b=3.9972(48)		α=γ=90°	
phase fraction 0.477					c= 4.0032(55)		β=91.023(270)	
phase 2(*P4mm*)								
Atoms	X	Y	Z	U_{iso}				
K/Na	0	0	0.0253(31)	0.0336(13)				
Nb	0.5	0.5	0.5137(4)	0.0056(6)				
O1	0.5	0.5	0.0536(9)	0.0124(7)				
O2	0.5	0	0.5572(6)	0.0067(5)				
Lattice parameter (Å)			α=β=γ=90°					
a= b=3.9588(2) c=4.0205(2)			phase fraction 0.523					

Rietveld and PDF refinement of KNN5 at 373 K

Rietveld refinement monoclinic phase (*Pm*)					PDF refinement monoclinic phase (*Pm*)			
Atoms	X	Y	Z	U_{iso}	X	Y	Z	U_{iso}
K/Na	-0.0064(20)	0	0.0251(26)	0.0157(4)	-0.0383 (50)	0	0.0293(85)	0.0161(30)
Nb	0.4727(5)	0.5	0.5300(6)	0.0034(2)	0.4822(1)	0.5	0.5329(2)	0.0081(10)
O1	0.5264(5)	0.5	0.0068(9)	0.0092(8)	0.5237(68)	0.5	-0.0029(27)	0.0183(23)
O2	-0.0026(10)	0.5	0.5167(12)	0.0107(7)	0.0154(1)	0.5	0.5089(2)	0.0061(10)
O3	0.4978(7)	0	0.4868(5)	0.0036(4)	0.5066(46)	0	0.4879(37)	0.0054(9)
Lattice parameter (Å)					Lattice parameter (Å)			
a= 4.0003(2)					a=3.9776(1)			
b=3.9465(2)		α=γ=90°			b= 3.9714(42)		α=γ=90°	
c=3.9905(2)		β=90.301(1)			c=4.0047(44)		β=90.663(18)	

Rietveld and PDF refinement of KNN5 at 290 K								
Rietveld refinement monoclinic phase (*Pm*)					PDF refinement monoclinic phase (*Pm*)			
Atoms	X	Y	Z	U_{iso}	X	Y	Z	U_{iso}
K/Na	-0.0041(18)	0	0.0205(26)	0.0137(3)	-0.0282(41)	0	0.0229(60)	0.0160(19)
Nb	0.4803(4)	0.5	0.5284(5)	0.0028(2)	0.4840(1)	0.5	0.5315(12)	0.0058(6)
O1	0.5334(5)	0.5	0.0010(8)	0.0083(7)	0.5269(38)	0.5	-0.0027(20)	0.0119(12)
O2	0.0071(8)	0.5	0.5117(10)	0.0086(6)	0.0181(1)	0.5	0.5081(27)	0.0086(10)
O3	0.5076(6)	0	0.4838(5)	0.0037(3)	0.5104(30)	0	0.4837(25)	0.0051(6)
Lattice parameter (Å)					Lattice parameter (Å)			
a=4.0024(2)					a=3.9631(1)			
b=3.9432(1)		α=γ=90°			b=3.9698(29)		α=γ=90°	
c=3.9930(2)		β=90.332(1)			c= 4.0181(30)		β=90.700(130)	

Rietveld and PDF refinement of KNN5 at 100 K

Rietveld refinement monoclinic phase (*Pm*)					PDF refinement monoclinic phase (*Pm*)			
Atoms	X	Y	Z	U_{iso}	X	Y	Z	U_{iso}
K/Na	-0.0036(16)	0	0.0301(19)	0.0082(4)	-0.0340(29)	0	0.0235(40)	0.0091(13)
Nb	0.4794(4)	0.5	0.5283(6)	0.0012(2)	0.4820(1)	0.5	0.5328(9)	0.0051(5)
O1	0.5326(7)	0.5	-0.0002(10)	0.0066(7)	0.5145(49)	0.5	-0.0051(19)	0.0131(10)
O2	0.0101(9)	0.5	0.5097(11)	0.0060(7)	0.0145(1)	0.5	0.5029(15)	0.0053(6)
O3	0.5101(7)	0	0.4844(6)	0.0022(3)	0.5098(25)	0	0.4829(18)	0.0029(4)
Lattice parameter (Å)					Lattice parameter(Å)			
a=4.0004(2)					a=3.9685(10)			
b=3.9382(2)		α=γ=90°			b=3.9569(23)		α=γ=90°	
c=3.9915(2)		β=90.364(2)			c= 4.0166(23)		β=90.577(94)	

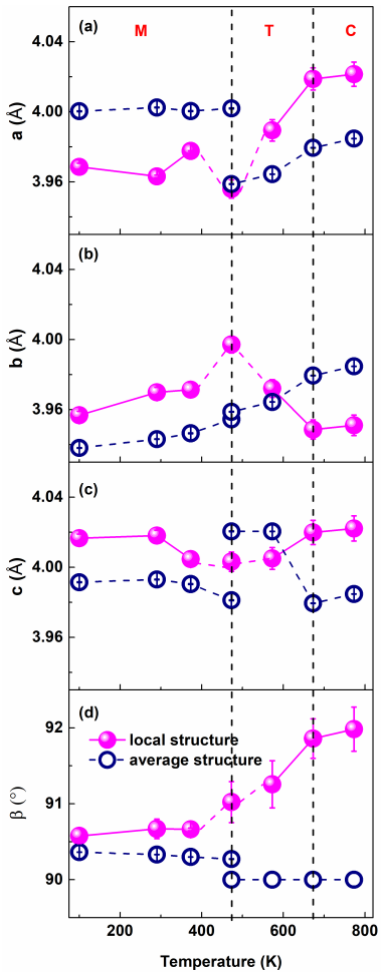

Figure 3

Units cell parameters for KNN5 as a function of temperature from 100 K to 773 K: (a) lattice parameter a; (b) lattice parameter b; (c) lattice parameter c; (d) interaxial angle β. Pink closed circles represent lattice parameters for the local structure from fits to *G*(*r*) of r~1.7-10 Å, while navy open circles represent lattice parameters for the average structure from Rietveld refinement of neutron diffraction patterns. Vertical dotted lines represent phase transition temperatures in average structure. The letters M, T and C mark the temperature range with the average phases of monoclinic, tetragonal, and cubic, respectively.

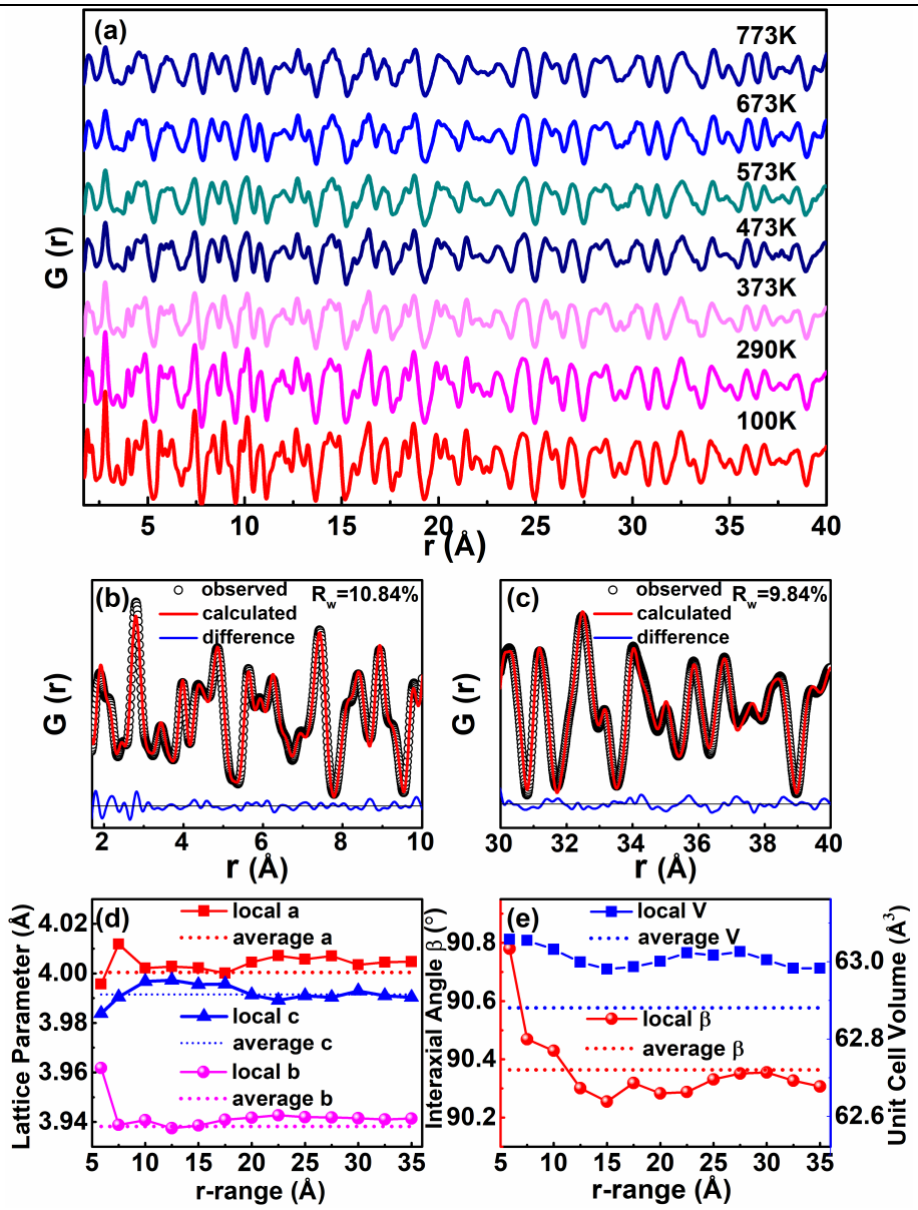

Figure 4

(a) Experimental G(*r*) with r~1.7-40 Å for KNN5 in the temperature range of 100 K ~773 K, showing the evolution of local and average structures. Note that the peak profile changes most significantly within r ~1.7-3 Å.(b-c) The fits to the experimental G(*r*) patterns at 100 K using *Pm* space group for different *r* ranges: (b) *r* ~ 1.7-10 Å, (c) *r* ~ 30-40 Å. (d-e) Evolution of structural parameters obtained from box-car fitting as a function of *r*: (d) lattice parameters a, b and c, (e) *a-c* interaxial angle β and unit cell volume V. The markers correspond to the parameters obtained from box-car refinements and the middle of the box, whereas the dotted lines correspond to the parameters from Rietveld refinement.

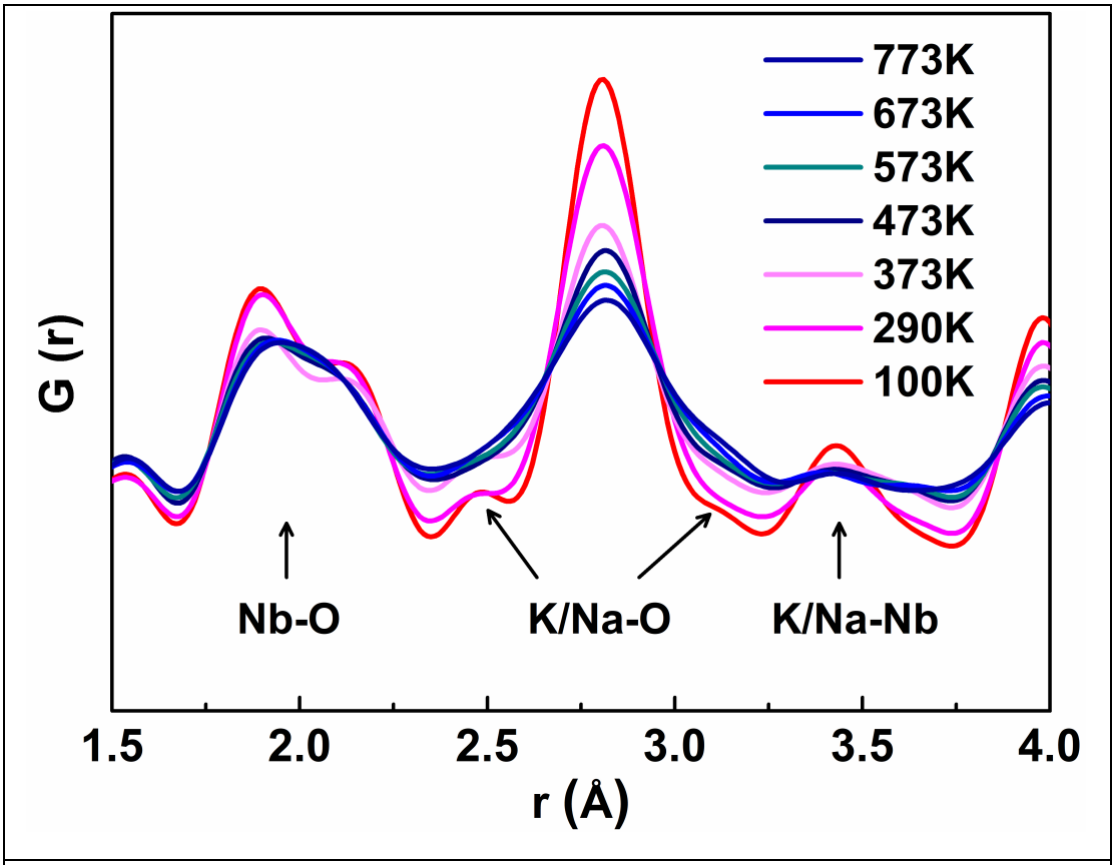

Figure 5

Temperature-dependent evolution of G(*r*), showing nearest neighbor pairwise atomic correlations. Peaks representing Nb-O, K/Na-O, and K/Na-Nb bond lengths are marked with arrows. Note that the profiles in red/pink (100 K-373 K) show a clear split in the nearest neighbor A-O and B-O peaks, while for profiles shown in blue (473 K-773 K) the peaks appear asymmetric without a clear split.

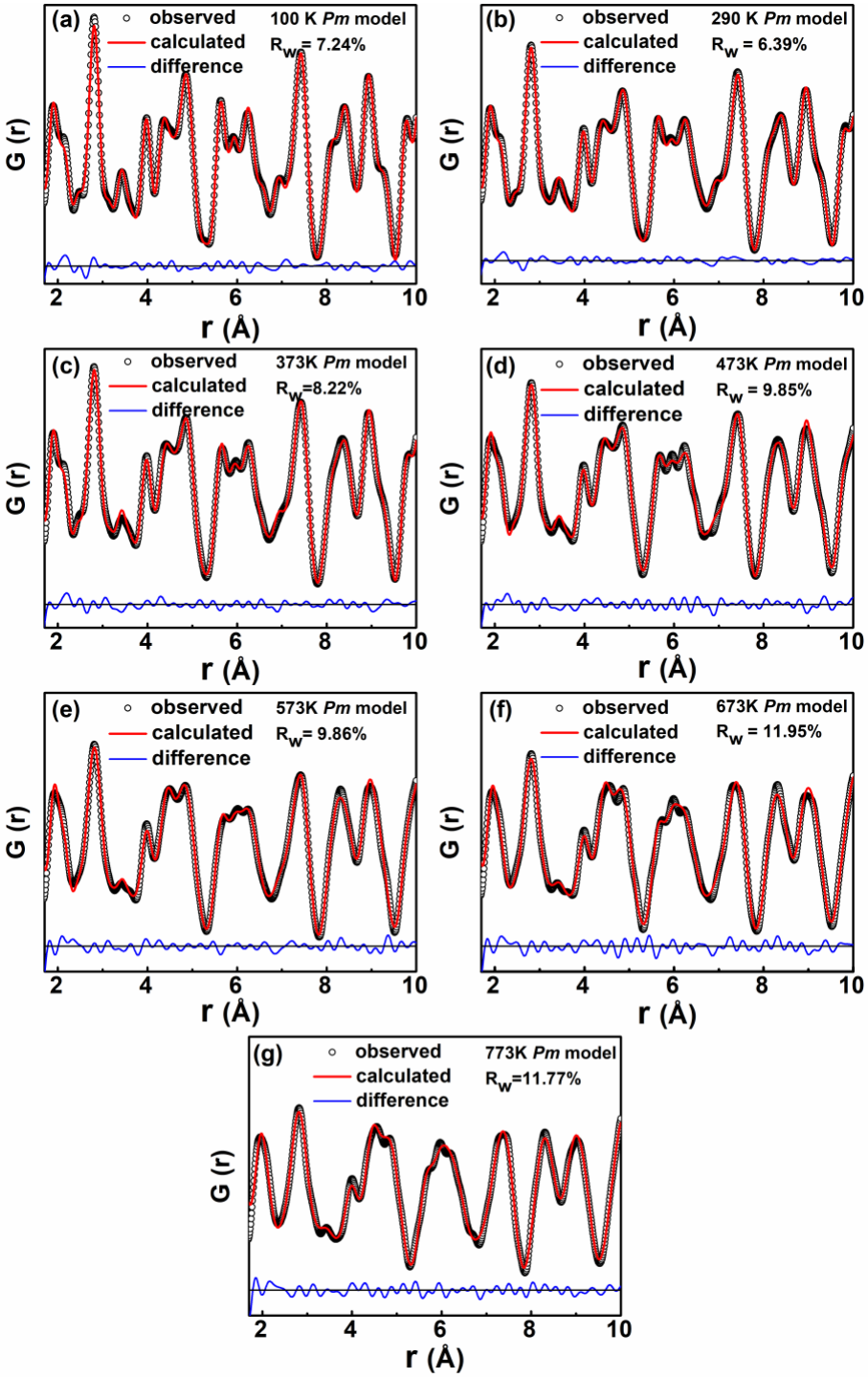

Figure 6

Experimental and fitted G(*r*) profiles of KNN5 for interatomic distance r < 10 Å, as a function of temperature: (a) 100K, (b) 290K, (c) 373K, (d) 473K, (e) 573K, (f) 673K, (g) 773K. The calculated profiles correspond to the fit obtained using a *Pm* space group, with starting parameters obtained from Rietveld analysis of the Bragg diffraction patterns at corresponding temperatures. R_w corresponds to the goodness of the fit at each temperature.

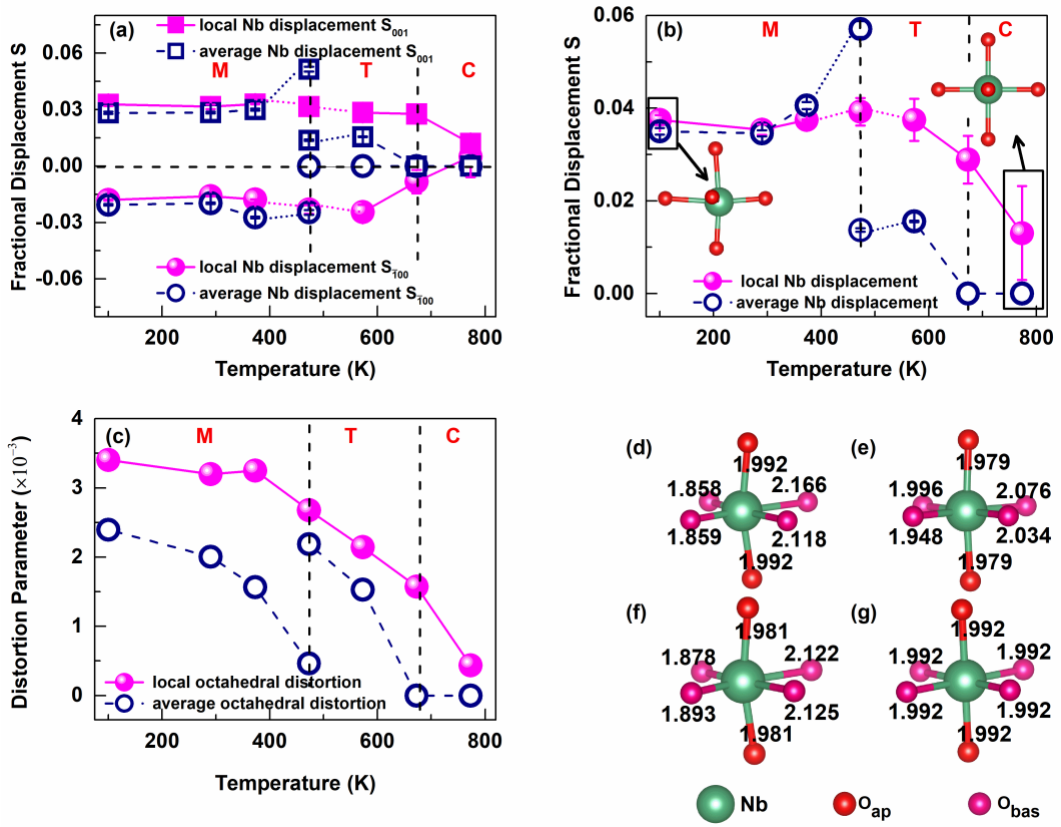

Figure 7

Atomic displacement and octahedral distortion as a function of temperature: (a) Nb fractional displacement along $\left[\bar{1}00\right]\left(S_{\bar{1}00}\right)$ and [001](S_{001}) directions, and (b) net Nb fractional displacement close to ~ $\left[\bar{1}01\right]$ or [001] direction, as a function of temperature from 100 K to 773 K, where insets are schemes of NbO_6 at 100 K and 773 K. Note that the Nb displacements are exaggerated for clarity. (c) Octahedral distortion parameter as a function of temperature from 100 K and 773 K for the local and average structures. Note that open symbols represent parameters obtained from average Rietveld refinement, while the closed symbols represent parameters obtained from PDF refinement in the range *r* ~1.7~10 Å. (d-e) Illustration of the NbO_6 octahedron in the local structure at 100 K (left top)) and 773 K (right top), respectively. (f-g) Illustration of the NbO_6 octahedron in the average structure at 100 K (left bottom) and 773 K (right bottom), respectively. The indicated Nb-O bond lengths in (d)-(g) are in the Angstroms (Å).

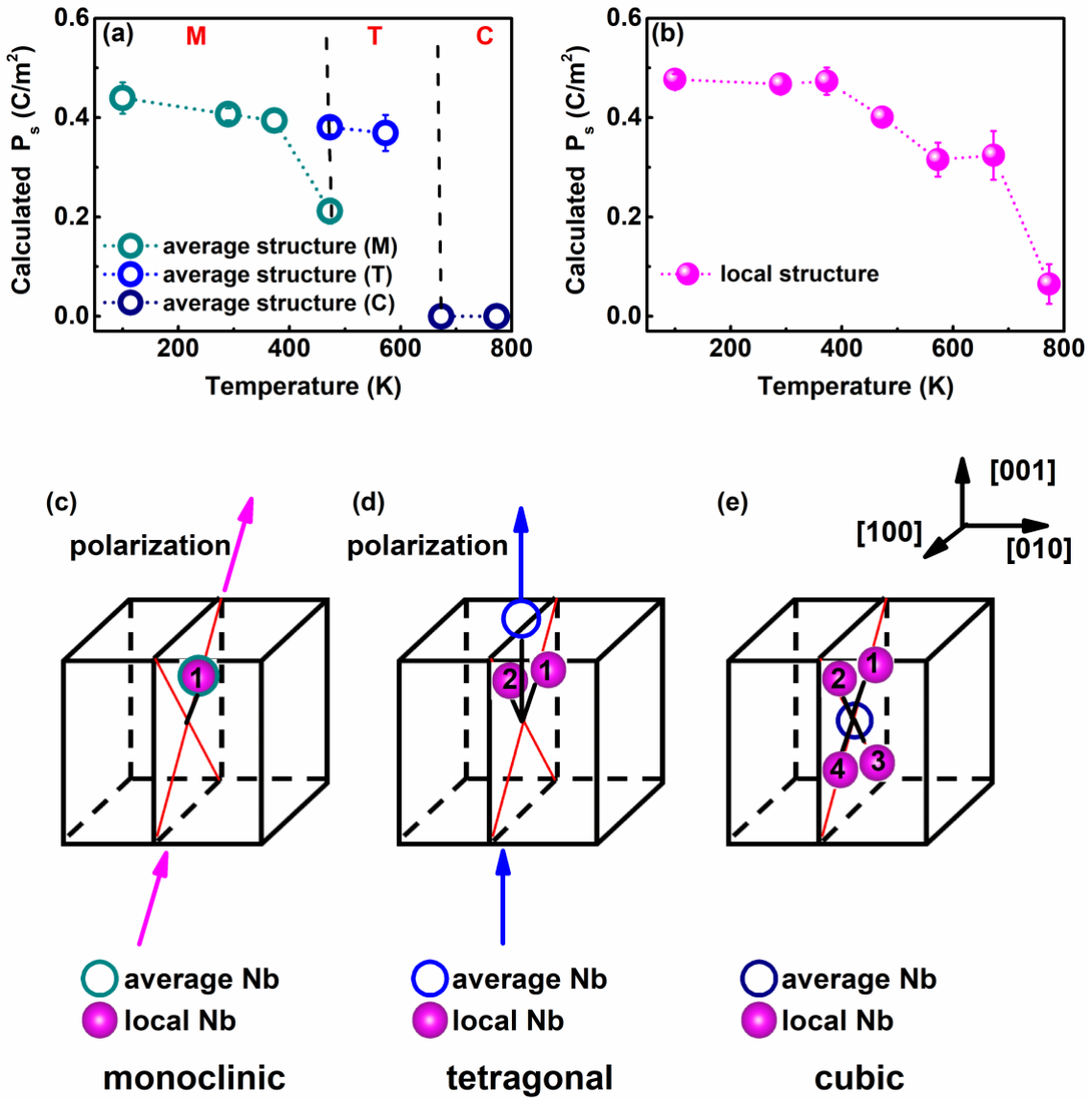

Figure 8

The calculated spontaneous polarization of KNN5 as a function of temperature, based on atomic positions in (a) the average structure, and (b) the local structure. The polarization for the local structure changes continuously with temperature, while a discontinuous change in the polarization for the average structure can be noted at the phase transition temperatures. The local atomistic mechanism for order-disorder type transition in KNN5 is schematically illustrated in (c)-(e). In (c)-(e), the closed circle represents Nb displacement in the local structure, while the open circle represents resultant displacement in the average structure. The line with an arrow represents the direction of the average polarization vector. Note that the Nb displacements are exaggerated for clarity.

References

[1] T. Zheng, J. Wu, D. Xiao, J. Zhu, Recent development in lead-free perovskite piezoelectric bulk materials, Prog. Mater. Sci. 98, 552 (2018).

[2] B. Jaffe, R. S. Roth, S. Marzullo, Piezoelectric properties of lead zirconate-lead titanate solid-solution ceramics, J. Appl. Phys. 25, 809 (1954).

[3] J. Wu, D. Xiao, J. Zhu, Potassium-sodium niobate lead-free piezoelectric materials: past, present, and future of phase boundaries, Chem. Rev. 115, 2559 (2015).

[4] L. Egerton, D. M. Dillon, Piezoelectric and dielectric properties of ceramics in the system potassium-sodium niobate, J. Am. Ceram. Soc. 42, 438 (1959).

[5] L. E. Cross, Electric double hysteresis in $(K_xNa_{1-x})NbO_3$ single crystals, Nature 181, 178 (1958).

[6] R. E. Jaeger, L. Egerton, Hot pressing of potassium-sodium niobates, J. Am. Ceram. Soc. 45, 209 (1962).

[7] V. J. Tennery, K. W. Hang, Thermal and X-ray diffraction studies of the $NaNbO_3$-$KNbO_3$ system, J. Appl. Phys. 39, 4749 (1968).

[8] B. Jaffe, W. R. Cook, H. Jaffe, *Piezoelectric Ceramics* (Academic Press, New York, 1971).

[9] J. Rödel, W. Jo, K. T. P. Seifert, E.-M. Anton, T. Granzow, D. Damjanovic, Perspective on the development of lead-free piezoceramics, J. Am. Ceram. Soc. 92, 1153 (2009).

[10] Y.-M. Li, Z.-Y. Shen, F. Wu, T.-Z. Pan, Z.-M. Wang, Z.-G. Xiao, Enhancement of piezoelectric properties and temperature stability by forming an MPB in KNN-based lead-free ceramics, J. Mater. Sci.-Mater. Electron. 25, 1028 (2014).

[11] P. Kumar, M. Pattanaik, Sonia, Synthesis and characterizations of KNN ferroelectric ceramics near 50/50 MPB, Ceram. Int. 39, 65 (2013).

[12] Y. Guo, K.-i. Kakimoto, H. Ohsato, Phase transitional behavior and piezoelectric properties of $(Na_{0.5}K_{0.5})NbO_3$–$LiNbO_3$ ceramics, Appl. Phys. Lett. 85, 4121 (2004).

[13] Z. Fu, J. Yang, P. Lu, L. Zhang, H. Yao, F. Xu, Y. Li, Influence of secondary phase on polymorphic phase transition in Li-doped KNN lead-free ceramics, Ceram. Int. 43, 12893 (2017).

[14] Y. Zhang, L. Li, B. Shen, and J. Zhai, Dalton transactions (Cambridge, England : 2003) 44, 7797 (2015).

[15] Y. Huan, X. Wang, Z. Shen, J. Kim, H. Zhou, L. Li, Nanodomains in KNN-based lead-free piezoelectric ceramics: origin of strong piezoelectric properties, J. Am. Ceram. Soc. 97, 700 (2014).

[16] M. Ahtee, A. M. Glazer, Lattice parameters and tilted octahedra in sodium–potassium niobate solid solutions, Acta Cryst. A 32, 434 (1976).

[17] H. Mgbemere, G. Schneider, M. Hoelzel, M. Hinterstein, Neutron diffraction study of $(K_xNa_{1-x})NbO_3$-based ceramics from low to high temperatures, J. Appl. Cryst.. 49, 891 (2016).

[18] K. Wang, F.-Z. Yao, W. Jo, D. Gobeljic, V. V. Shvartsman, D. C. Lupascu, J.-F. Li, J. Rödel, Temperature-insensitive (K,Na)NbO3-based lead-free piezoactuator ceramics, Adv. Funct. Mater. 23, 4079 (2013).

[19] D. W. Baker, P. A. Thomas, N. Zhang, A. M. Glazer, Structural study of $K_xNa_{1-x}NbO_3$ (KNN) for compositions in the range x=0.24-0.36, Acta Crystallogr. Sect. B 65, 22

(2009).
[20] D. W. Baker, P. A. Thomas, N. Zhang, A. M. Glazer, A comprehensive study of the phase diagram of $K_xNa_{1-x}NbO_3$, Appl. Phys. Lett. 95, 91903 (2009).
[21] V. Petkov, J.-W. Kim, S. Shastri, S. Gupta, S. Priya, Geometrical frustration and piezoelectric response in oxide ferroics, Phys. Rev. Materials 4, 014405 (2020).
[22] W. Ge, Y. Ren, J. Zhang, C. P. Devreugd, J. Li, D. Viehland, A monoclinic-tetragonal ferroelectric phase transition in lead-free $(K_{0.5}Na_{0.5})NbO_3$-x%$LiNbO_3$ solid solution, J. Appl. Phys. 111, 103503 (2012).
[23] S. Gupta, V. Petkov, S. Priya, Local atomic structure of $K_xNa_{(1-x)}NbO_3$ by total x-ray diffraction, Appl. Phys. Lett. 105, 232902 (2014).
[24] R. D. Shannon, Revised effective ionic radii and systematic studies of interatomic distances in halides and chalcogenides, Acta Cryst. A 32, 751 (1976).
[25] A. Kodre, J. Tellier, I. Arčon, B. Malič, M. Kosec, Extended x-ray absorption fine structure study of phase transitions in the piezoelectric perovskite $K_{0.5}Na_{0.5}NbO_3$, J. Appl. Phys. 105, 113528 (2009).
[26] I. Levin, V. Krayzman, G. Cibin, M. G. Tucker, M. Eremenko, K. Chapman, R. L. Paul, Coupling of emergent octahedral rotations to polarization in (K,Na)NbO_3 ferroelectrics, Sci. Rep. 7, 15620 (2017).
[27] T. Egami, S. J. L. Billinge, *Underneath the Bragg peaks: structural analysis of complex materials* (Elsevier, 2003).
[28] I.-K. Jeong, T. W. Darling, J. K. Lee, T. Proffen, R. H. Heffner, J. S. Park, K. S. Hong, W. Dmowski, T. Egami, Direct observation of the formation of polar nanoregions in $Pb(Mg_{1/3}Nb_{2/3})O_3$ using neutron pair distribution function analysis, Phys. Rev. Lett. 94, 147602 (2005).
[29] S. Teslic, T. Egami, D. Viehland, Local atomic structure of PZT and PLZT studied by pulsed neutron scattering, J. Phys. Chem. Solids 57, 1537 (1996).
[30] W. Dmowski, M. K. Akbas, P. K. Davies, T. Egami, Local structure of $Pb(Sc_{1/2},Ta_{1/2})O_3$ and related compounds, J. Phys. Chem. Solids 61, 229 (2000).
[31] T. Egami, Temperature dependence of the local structure in Pb containing relaxor ferroelectrics, in: *AIP Conference Proceedings* (AIP, Williamsburg, 2003), p. 48–54.
[32] L. Jiang, D. C. Mitchell, W. Dmowski, T. Egami, Local structure of $NaNbO_3$: A neutron scattering study, Phys. Rev. B 88, 2171 (2013).
[33] E. Aksel, J. S. Forrester, J. C. Nino, K. Page, D. P. Shoemaker, J. L. Jones, Local atomic structure deviation from average structure of $Na_{0.5}Bi_{0.5}TiO_3$: Combined x-ray and neutron total scattering study, Phys. Rev. B 87, 2651 (2013).
[34] V. Petkov, M. Gateshki, M. Niederberger, Y. Ren, Atomic-scale structure of nanocrystalline $Ba_xSr_{1-x}TiO_3$ (x = 1, 0.5, 0) by X-ray diffraction and the atomic pair distribution function technique, Chem. Mater. 18, 814 (2006).
[35] B. H. Toby, R. B. von Dreele, GSAS-II the genesis of a modern open-source all purpose crystallography software package, J. Appl. Cryst.. 46, 544 (2013).
[36] L. B. McCusker, R. B. von Dreele, D. E. Cox, D. Louër, P. Scardi, Rietveld refinement guidelines, J. Appl. Cryst. 32, 36 (1999).

[37] see Supplementary Information for additional details on fitting of neutron diffraction and PDF data, and calculation of electrical polarization

[38] T.-M. Usher, T. Iamsasri, J. S. Forrester, N. Raengthon, N. Triamnak, D. P. Cann, J. L. Jones, Local and average structures of $BaTiO_3$-$Bi(Zn_{1/2}Ti_{1/2})O_3$, J. Appl. Phys. 120, 184102 (2016).

[39] S. Venkateshwarlu, S. Nayak, F. P. Marlton, F. Weyland, N. Novak, D. Maurya, Y. Veerabhadraiah, O. Borkiewicz, K. A. Beyer, M. R. V. Jørgensen, A. Pramanick, Relaxor behavior and electrothermal properties of Sn- and Nb-modified $(Ba,Ca)TiO_3$ Pb-free ferroelectric, J. Mater. Res. 35, 1017 (2020).

[40] C. L. Farrow, P. Juhas, J. W. Liu, D. Bryndin, E. S. Božin, J. Bloch, T. Proffen, S. J. L. Billinge, PDFfit2 and PDFgui: computer programs for studying nanostructure in crystals, J. Phys. Condens. Matter 19, 335219 (2007).

[41] M. D. Fontana, G. Metrat, J. L. Servoin, F. Gervais, Infrared spectroscopy in $KNbO_3$ through the successive ferroelectric phase transitions, J. Appl. Phys. 17, 483 (1984).

[42] R. E. Cohen, H. Krakauer, Lattice dynamics and origin of ferroelectricity in $BaTiO_3$: Linearized-augmented-plane-wave total-energy calculations, Phys. Rev. B Condens. Matter 42, 6416 (1990).

[43] R. Comes, M. Lambert, A. Guinier, The chain structure of $BaTiO_3$ and $KNbO_3$, Solid State Commun. 6, 715 (1968).

[44] R. Comès, M. Lambert, A. Guinier, Désordre linéaire dans les cristaux (cas du silicium, du quartz, et des pérovskites ferroélectriques), Acta Cryst. A 26, 244 (1970).

[45] L. Veselinović, M. Mitrić, M. Avdeev, S. Marković, D. Uskoković, New insights into $BaTi_{1-x}Sn_xO_3$ ($0 \leq x \leq 0.20$) phase diagram from neutron diffraction data, J. Appl. Cryst. 49, 1726 (2016).

[46] A. W. Hewat, Cubic-tetragonal-orthorhombic-rhombohedral ferroelectric transitions in perovskite potassium niobate: neutron powder profile refinement of the structures, J. Phys. C: Solid State Phys. 6, 2559 (1973).

[47] A. W. Hewat, Soft modes and the structure, spontaneous polarization and Curie constants of perovskite ferroelectrics: tetragonal potassium niobate, J. Appl. Phys. 6, 1074 (1973).

[48] X. Sun, J. Deng, J. Chen, C. Sun, X. Xing, Effects of Li substitution on the structure and ferroelectricity of (Na, K)NbO_3. J. Am. Ceram. Soc. 92, 3033 (2009).

[49] C. Malibert, B. Dkhil, J. M. Kiat, D. Durand, J. F. Bérar, A. S.-d. Biré, Order and disorder in the relaxor ferroelectric perovskite $PbSc_{1/2}Nb_{1/2}O_3$ (PSN): comparison with simple perovskites $BaTiO_3$ and $PbTiO_3$, J. Phys. Condens. Matter 9, 7485 (1997).